Chemical Engineering Science 269 (2023) 118458

Contents lists available at ScienceDirect

Chemical Engineering Science

journal homepage: www.elsevier.com/locate/ces

A bubble coalescence kernel combining the characteristics of the film drainage, energy, and critical velocity models

Suat Canberk Ozan [a,b,*], Jannike Solsvik [a], Hugo Atle Jakobsen [a]

[a] Department of Chemical Engineering, Norwegian University of Science and Technology (NTNU), Trondheim, Norway
[b] SINTEF Industry, Process Technology Department, Trondheim, Norway

HIGHLIGHTS

- A novel coalescence kernel is constructed.
- Kernel combines characteristics of film drainage, energy and critical velocity models.
- Collision parameters are handled through probability distributions.
- Kernel is free of adjustable tuning parameters.
- Kernel predictions match experimental results well.

ARTICLE INFO

Article history:
Received 31 October 2022
Received in revised form 1 January 2023
Accepted 4 January 2023
Available online 7 January 2023

Keywords:
Coalescence probability
Coalescence frequency
Film drainage
Critical velocity
Coalescence kernel

ABSTRACT

A novel coalescence kernel with high predictive properties is constructed to be used within the population balance framework. The kernel includes the product of a collision frequency term and a novel binary coalescence probability expression. The probability expression employs critical velocity estimations from film drainage simulations that also considers particle surface and kinetic energies. Thus, the proposed expression possesses characteristics of all three commonly used approaches: film drainage, energy, and critical velocity models. The probability of a collision having a certain velocity and angle is considered through probability density functions while adapting to the Eulerian frame. A maximum collision angle that allows coalescence is defined. The kernel is free of artificially introduced tuning parameters and predicts the size distributions in bubbly pipe flow experiments exceptionally well, including complex behaviors such as emergence of secondary peaks in the distribution. The theory presented is equally valid for bubbles and droplets.

1. Introduction

Coalescence is the phenomenon where two or more fluid particles, i.e., bubbles or droplets, merge and form a new one. Coalescence plays a crucial role in many natural phenomena and in industrial applications where dispersed multiphase flows are frequently encountered. In the latter, the spatial distribution and the size distribution of the dispersed phase are important variables that can affect the overall efficiency of the process. For example, in a separation unit, coalescence may be desired for increased efficiency, as the larger particles are typically easier to separate; whereas in a chemical reactor, smaller particles with higher surface area to volume ratios are more beneficial in diminishing mass transfer limitations and improving the overall reaction rates. Therefore, accurate coalescence kernels with high predictive properties are essential for chemical engineering and multiphase flow communities.

The population balance framework is widely used in dispersed flow modelling, in which the effect of coalescence (and breakage) comes into play via source and sink terms that represent the birth of a new fluid particle and the death of the original ones, respectively. A coalescence frequency expression is employed as a part of these source/sink terms. A common approach is to express the coalescence frequency as a product of the collision frequency, i.e., how often the fluid particles get into contact within the dispersed flow, and the coalescence probability of the interacting fluid particles. Three main branches of coalescence probability models exist in the literature (Liao and Lucas, 2010): the film drainage approach, the energy models, and the critical approach velocity model. The film drainage approach relates the probability to the ratio between

* Corresponding author at: Department of Chemical Engineering, Norwegian University of Science and Technology (NTNU), Trondheim, Norway.
E-mail address: canberk.ozan@sintef.no (S.C. Ozan).

https://doi.org/10.1016/j.ces.2023.118458
0009-2509/

two time scales (Coulaloglou, 1975), one representing the duration for which particles can stay in contact and the other showing the time required for the two particles to coalesce. The latter time scale is then commonly estimated through hydrodynamic modelling of the draining film in between the two colliding particles. The energy models pioneered by Sovova (1981) on the other hand, expresses the coalescence probability by comparing the surface energy of the particles to their kinetic energy during the collision. The final approach stems from the experimental observations of Lehr et al. (2002) and claims that two particles can only coalesce when their relative approach velocity is below a critical value. Although all three approaches have merit and applicability in certain configurations, they also have a few drawbacks. For example, the film drainage based models assume that the particle interactions and the drainage of the film are two independent phenomena, which is unlikely to be true in reality, and calculate the two required time scales with two different models that can be based on conflicting arguments. The energy models indicate increasing coalescence probability with relative collision velocity, whereas experiments show the existence of a maximum velocity that allows coalescence (Duineveld, 1998;Lehr et al., 2002). The critical approach velocity model requires tedious experimental work for measuring the critical velocity under different flow conditions. Perhaps more importantly, many models proposed in the literature require tuning parameters that can often be small or large enough to change the order of magnitude of the estimated coalescence frequency.

In a more recent work, Das (2015) criticizes the fact that the collision frequency and the coalescence probability are treated independently, and proposes a new framework in which the coalescence frequency is developed as a single entity instead of the product of the two. This framework does not treat the relative collision velocity as a single value but instead assigns a probability distribution to it, and eventually requires comparison between the approach velocity and a critical velocity to determine the coalescence probability. A similar framework with more in depth turbulence induced collision mechanisms is proposed by Gong et al. (2018). In both works, the critical velocity is determined by equating the interaction time and coalescence time scales proposed by Kamp et al. (2001). In other words, just as it is done in the film drainage based coalescence probability models, the particle interaction and the coalescence are handled as two separate phenomena. To avoid this, Ozan et al. (2021) suggest a new framework that allows the critical approach velocity to be estimated directly from the hydrodynamic film drainage simulations. In the hydrodynamic modelling, the two colliding particles are typically assumed to approach each other either at a constant velocity (Klaseboer et al., 2000; Ozan and Jakobsen, 2019a) or with a constant interaction force (Bazhlekov et al., 2000), meaning that there is no possibility for the reversal of the drainage in these typical models and consequently they cannot estimate the rebound of the particles. By solving a force balance over the fluid particles simultaneously with the hydrodynamic drainage model, Ozan et al. (2021) allow the relative approach velocity to be time dependent. If the film's resistance to drainage becomes significant enough, the velocity attains negative values and the reversal of the drainage begins. In turn, this capability in the model enables the estimation of the collision outcome either as coalescence or rebound within a single simulation without requiring additional estimations, e.g. for an interaction time scale. Then, a critical velocity separating the coalescence and the rebound regimes for a given parameter set is estimated through the simulations. As this model estimates critical approach velocities through hydrodynamic film drainage simulations that also incorporate the effects of the particle surface and kinetic energies (via the force balance), a novel coalescence kernel based on Ozan et al. (2021)'s work can potentially carry the positive aspects of all the three approaches for coalescence frequency estimations existing in the literature. Furthermore, this kernel would avoid inheriting their drawbacks, since, e.g., it does not assume independent interaction and coalescence phenomena or since it matches the experimental observations in estimating rebound at larger velocities unlike the energy models. The current work uses the estimated critical velocities to construct such a novel kernel. The proposed framework also handles the relative approach velocity of the particles and the collision angle as variables with probability distributions to adapt the observations on a single collision event to be used in an Eulerian framework.

The model development is presented in Section 2: the critical velocity and the coalescence probability of a single collision event are considered in Section 2.1, followed by the relative velocity distribution between two fluid particles in a flow field in Section 2.2, and the coalescence frequency expression in Section 2.3. The outcomes of the proposed probability and frequency expressions are presented and discussed in Section 3.1. In Section 3.2, the novel coalescence kernel is integrated into an Eulerian multifluid-population balance model and its predictions are compared to bubbly pipe flow experiments. Finally, Section 4 presents the conclusions.

2. Model development

In the population balance framework, to express the effect of coalescence in fluid particle size and distribution within a dispersed flow, it is customary to use coalescence frequency as a product of the collision frequency and the coalescence probability, respectively indicating how often two fluid particles collide, and how probable the given collision results in coalescence. Then, in analogy with the kinetic theory of gases, the collision frequency is written as the product of the collision cross-sectional area, $S = \frac{\pi}{4}(d_\xi + d_\eta)^2$, and the relative velocity between the particles, v_{rel}, for fluid particles of sizes d_ξ and d_η. For the coalescence probability on the other hand, there are three main approaches in the literature (Liao and Lucas, 2010): the film drainage approach, the energy models, and the critical approach velocity model. The current work proposes a new methodology for determining the coalescence probability, and consequently the coalescence frequency, based on the results of Ozan et al. (2021), which combines some of the positive characteristics of the existing film drainage, enery and critical velocity models. In what follows, we will discuss how this coalescence kernel is built and its application in the Eulerian and Lagrangian modelling of dispersed flows.

2.1. Critical velocity and coalescence probability

Ozan et al. (2021) study the film drainage between two fluid particles with freely-deforming interfaces that can support dimple formation by considering a time dependent relative approach velocity. The time dependent behavior of v_{rel} is governed by a force balance that accounts for the changes in the kinetic and the particle surface energies. The time dependent v_{rel} can attain negative values when the film's resistance to the drainage is large enough, signifying the onset of rebound of the particles. Thus, in addition to predicting coalescence, the drainage model is able to estimate the rebound. This in turn means that for a given parameter set the outcome of the collision can be predicted as either coalescence or rebound within a single simulation without requiring secondary models/estimations. Then, the largest initial v_{rel} value that allows coalescence (or the smallest that allows rebound) is denoted as the critical relative approach velocity v_c of the corresponding parameter set. In their Fig. 10, Ozan et al. (2021) present v_c as a function of the equivalent particle radius, $R_p = (1/d_\xi + 1/d_\eta)^{-1}$, for air-in-water systems with immobilized interfaces, which is a

common occurrence in many real systems. In the current work, the modelling efforts start based on this data. A curve fit on the v_c data gives

$$\frac{v_c \mu_c}{\sigma} = 7.25 \times 10^{-7} R_p^{-0.89} \tag{1}$$

where R_p is in m, and μ_c and σ are the continuous phase viscosity and the system interfacial tension, respectively. The v_c data yielding Eq. (1) are obtained by assuming an initial minimum film thickness of $h_{00} = 0.1R_p$. However, the v_c values are found to be relatively insensitive to the changes in h_{00} used in the film drainage simulations, as can be seen in Fig. 1. As a result, the v_c expression itself does not change with h_{00} significantly. For example, for $h_{00} = 0.5R_p$,

$$\frac{v_c \mu_c}{\sigma} = 8.24 \times 10^{-7} R_p^{-0.90} \tag{2}$$

The v_c expression can be directly adopted in models where the exact velocity of each particle is known, for example in Lagrangian simulations, to estimate the collision outcome. However, it must be noted that the reported velocity values here are the projections of the velocity vectors on the line of impact during a collision, since Ozan et al. (2021) considers only axisymmetric collisions. In reality, the probability of having a perfectly head-on collision, such that the line of impact and $\mathbf{v}_{rel}$ coincide, is virtually zero. Therefore, the impact of the collision angle α should also be taken into consideration. As sketched in Fig. 2, α is defined such that $\alpha = 0^\circ$ correspond to a perfectly head-on collision, and when $\alpha = 90^\circ$ the particles barely miss each other. The $\mathbf{v}_{rel}$ component along the line of impact is given by $v_{rel} \cos\alpha$, and it is the one corresponding to the approach velocity in the film drainage simulations. Then, the coalescence probability of a single collision is given by

$$P = \begin{cases} 1, & \text{if } v_{rel} \cos\alpha < v_c(R_p), \quad 0 \leqslant \alpha < 90^\circ \\ 0, & \text{if } v_{rel} \cos\alpha \geqslant v_c(R_p), \quad 0 \leqslant \alpha < 90^\circ \end{cases} \tag{3}$$

Although this formulation is reasonable for head-on collisions and for collisions with moderate collision angles, when α is large it erroneously estimates coalescence even at extremely high velocities since $\cos\alpha$ is small. To avoid this, α_u, an upper limit for coalescence to possibly occur, is introduced:

$$P = \begin{cases} 1, & \text{if } v_{rel} \cos\alpha < v_c(R_p) \quad \text{and} \quad \alpha < \alpha_u \\ 0, & \text{otherwise} \end{cases} \tag{4}$$

The existence of such an upper limit can be found in the literature, e.g., according to Rother et al. (1997) $\alpha_u = 1.019$ radians $\approx 58^\circ$.

In many configurations, it is not computationally feasible to completely resolve the dispersed flow and Eulerian simulations are employed, in which the precise information on the position and the velocity of the individual particles is unavailable. In this case, the velocity of the particles should be estimated through a probability density function instead of assuming it is a single known value.

2.2. Fluid particle velocity distribution

Wilczek et al. (2011) observe that the fluid velocities in isotropic turbulence is Gaussian distributed. Based on this observation, it is possible to determine a probability distribution for the relative velocity between two fluid particles (Das, 2015;Gong et al., 2018). As shown in Appendix A, the probability density function for v_{rel} between two particles of sizes d_ξ and d_η is given by:

$$f_{v_{rel}} = \frac{4\pi v_{rel}^2}{\left[2\pi\left(\sigma_\xi^2 + \sigma_\eta^2\right)\right]^{3/2}} \exp\left(-\frac{1}{2}\frac{v_{rel}^2}{\sigma_\xi^2 + \sigma_\eta^2}\right) \tag{5}$$

Furthermore, the variances σ_ξ^2 and σ_η^2 are required to determine the density function. By considering the inertial subrange of turbulence, Das (2015) argues that v_{rel} between two particles of size d_ξ can be approximated with $(\epsilon d_\xi)^{1/3}$ at their point of impact, where ϵ is the dissipation rate. A full-spectrum approach is discussed by Solsvik and Jakobsen (2016). Their Eqs. (81)-(87) read

$$[\delta v]^2 = \frac{4}{3} k\{1 - [T_1 + T_2(T_3 T_4 - T_5)]\} \tag{6}$$

where

$$T_1 = \frac{2}{s^2} F\left(\left(-\frac{1}{3}\right)^{1/2}, \left(\frac{3}{2}\right), \frac{s^2}{4}\right) \tag{7}$$

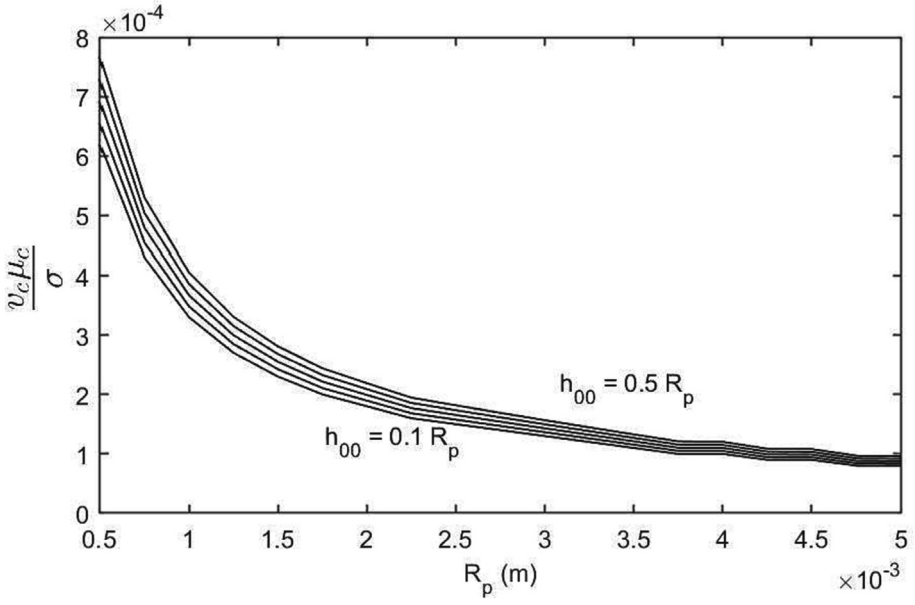

Fig. 1. Dimensionless critical velocity as a function of $R_p(m)$ obtained by considering different initial separation thicknesses in film drainage simulations. The minimum initial thickness values are $h_{00} = [0.1, 0.2, 0.3, 0.4, 0.5] \times R_p$.

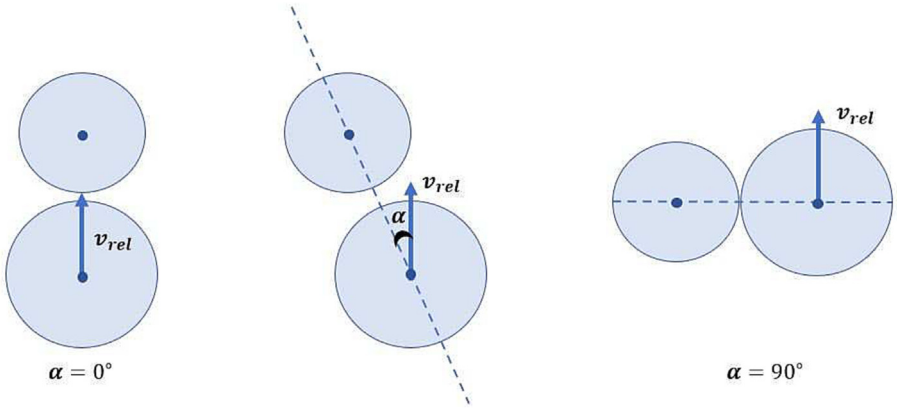

Fig. 2. Sketch of the collision geometry.

$$T_2 = 3^{3/2}\Gamma(2/3) \tag{8}$$

$$T_3 = 27s^{2/3}2^{1/3}\Gamma(2/3) \tag{9}$$

$$T_4 = \frac{1}{352\pi}F\left(\left(\frac{7}{3}\right)^{11/6}, \left(\frac{17}{6}\right), \frac{s^2}{4}\right) \tag{10}$$

$$T_5 = \frac{1}{2\pi}\left(\frac{2}{s}\right)^{2/3}K_{\frac{4}{3}}(s) \tag{11}$$

and

$$s = \kappa r/\left(c_L^{-1/2}\kappa L\right) \tag{12}$$

F, K and Γ are the hypergeometric, the Bessel, and the gamma functions respectively. L is the integral length scale (taken as the pipe diameter during the comparison with bubbly flow experiments), k is the turbulent kinetic energy, r can be approximated as the fluid particle size, and c_L is given as a function of Kolmogorov parameter C as (Solsvik, 2017):

$$c_L = \exp\left[-\frac{4.478 + 18.362C}{Re_\lambda^{1.075-0.070C}} - 1.342 + 2.024C\right] - 1.913 + 2.169C \tag{13}$$

where the Taylor-scale Reynolds number is

$$Re_\lambda = \sqrt{\frac{20}{3}}\sqrt{\frac{k^2}{\epsilon\nu_L}} \tag{14}$$

with ν_L being the continuous phase kinematic viscosity.

The resulting δv from Eqs. (6)–(14) can be taken as an indicator of the relative velocity between two particles upon their impact in a similar fashion to Das (2015)'s estimation. The same quantity can also be determined through Eq. (5). For two fluid particles of same size, Eq. (5) reduces to

$$f_{v_{rel}} = \frac{v_{rel}^2}{\sqrt{4\pi}\sigma_\xi^3}\exp\left(-\frac{1}{4}\frac{v_{rel}^2}{\sigma_\xi^2}\right) \tag{15}$$

whose expected value is given by

$$E\left[f_{v_{rel}}\right] = \int_0^\infty v_{rel}f_{v_{rel}}dv_{rel} = \frac{4}{\sqrt{\pi}}\sigma_\xi \tag{16}$$

By combining the two estimations, i.e., by assuming $E[f_{v_{rel}}] \approx \delta v$, the standard deviation is found as

$$\sigma_\xi = \sqrt{\frac{\pi}{12}k\{1 - [T_1 + T_2(T_3T_4 - T_5)]\}} \tag{17}$$

The same equation holds for σ_η as well, since $f_{v_{rel}}(\sigma_\eta, \sigma_\xi) = f_{v_{rel}}(\sigma_\xi, \sigma_\eta)$. By considering a vertical pipe (as such a configuration is employed for model validation in Section 3.2) with a diameter of D_{pipe}, the turbulent kinetic energy is obtained through $k = (D_{pipe}\epsilon)^{2/3}$, and the turbulent energy dissipation rate ϵ is estimated following Eq. (13) of Zhao et al. (2021):

$$\varepsilon = 1.21 \times 10^{-4}\left(\frac{j_G + j_L}{\nu_L}D_{pipe}\right)^{-0.25}\left(\frac{j_G}{j_L}\right)^{-0.5}\frac{2j_L^3}{D_{pipe}} \tag{18}$$

where j_G and j_L are the superficial gas and liquid velocities.

As the coalescence probability of a single collision (Eq. (4)) and the probability density function of v_{rel} (Eq. (5)) are determined, the coalescence frequency for an Eulerian model will be estimated next.

2.3. Coalescence frequency

For a pair of fluid particles with sizes d_ξ and d_η with a known v_{rel} the coalescence frequency can be written as

$$C(d_\xi, d_\eta) = S(d_\xi, d_\eta)\, v_{rel}\, P(d_\xi, d_\eta, v_{rel}, v_c, \alpha) \tag{19}$$

where the product of $S = \frac{\pi}{4}(d_\xi + d_\eta)^2$ and v_{rel} gives the swept volume rate, which represents the collision frequency, and P is the coalescence probability (given that the collision occurs) defined in Eq. (4). However, the collision angle and v_{rel} are not necessarily known constant values, and their probability density functions $f_{v_{rel}}$ and f_α should be included in the expression. Then, this expression should be integrated over the whole v_{rel} and α ranges to take all possible states into consideration. This yields

$$\mathbb{C}(d_\xi, d_\eta) = \frac{\pi}{4}(d_\xi + d_\eta)^2\int_0^\infty\int_0^{\pi/2} v_{rel}f_\alpha f_{v_{rel}}(d_\xi, d_\eta, v_{rel})\, P(d_\xi, d_\eta, v_{rel}, v_c, \alpha)\, d\alpha\, dv_{rel} \tag{20}$$

Here the product of the collision cross-sectional area and v_{rel} indicates the frequency of collisions in the flow field, f_α and $f_{v_{rel}}$ give the probabilistic distributions for the collision conditions, the angle and the relative velocity, and P is the coalescence probability of a collision to result in coalescence under these conditions. By assuming one of the particles is in a frozen frame, and the other's relative position with respect to the first particle has a uniform probability distribution, the probability of having a collision with $\alpha = \alpha_0$, where $0 \leqslant \alpha_0 \leqslant \pi/2$, follows $f_\alpha = \sin(2\alpha)$. Although all possible α values are taken into consideration in Eq. (20), notice that the probability expression (Eq. (4)) enforces an upper integration limit for α as discussed in Section 2.1. In the following section, the validity and the performance of the proposed coalescence closure are tested.

3. Results and discussion

This section first presents and discusses the outcomes of the probability expressions developed in Section 2; and then evaluates the validity and the predictive performance of the coalescence frequency expression (Eq. (20)) against the bubbly pipe flow experiments of Lucas et al. (2011). Lucas et al. (2011) is an internal report where the raw experimental data from Lucas et al. (2005) were re-evaluated through an improved methodology. The experimental parameters for the three runs (96, 107, 108) used in the current study is given in Table 1. To simulate the bubbly pipe flow, an Eulerian multifluid-population balance model is employed with Eq. (20) as the coalescence frequency. The details of the population balance model is given in Section 5.2 of Solsvik and Jakobsen (2014) and the final equations used in the current work is presented in Appendix B.

It must be noted that, even though the experimental validation is only done for a gas–liquid system in Section 3.2, the theory presented so far and the results of Section 3.1 are equally valid for both bubbles and droplets.

3.1. Outcome of the probability expressions

The relative velocity probability density function (as given in Eq. (5)) is presented in Fig. 3 for different particle size couples, where the variance is calculated through Eq. (16). The physical parameters are taken from the run 107 of Lucas et al. (2005) throughout this subsection. The results indicate that both the attainable relative velocity values and v_{rel} with largest probability increase with increasing particle sizes. In other words, larger fluid particles are more likely to collide with higher v_{rel}. Additionally, the threshold for their rebound (v_c) is also smaller as can be seen through Eq. (1). Thus, the likelihood of coalescence decreases with the equivalent particle size.

Table 1
Experimental runs employed in model validation and the relevant parameters (Lucas et al., 2011).

Run	j_G (m/s)	j_L (m/s)	D_{pipe} (mm)	L_{pipe} (m)
96	0.0898	1.017	51.2	3.5
107	0.140	1.017	51.2	3.5
108	0.140	1.611	51.2	3.5

The relative collision velocity and v_c are not the only factors affecting the coalescence probability and the impact of the collision angle α should also be considered. By momentarily disregarding the upper limit for α, the coalescence behavior map for a given particle size pair can be obtained by calculating the root of Eq. (3), i.e., the solution for $v_{rel}\cos\alpha = v_c(R_p)$. Fig. 4 shows the solution for a fixed d_η of 1 mm and different d_ξ as a function of α and v_{rel}, where each curve separates the coalescence (below the curve) and the no-coalescence (above the curve) regions for the corresponding particle sizes. In addition to confirming the earlier observation regarding the relation between the likelihood of coalescence and particle sizes, Fig. 4 also reveals that as a collision gets closer to being head-on (decreasing α), it requires a lower v_{rel} for coalescence to occur. This behavior can be explained by analyzing the components of v_{rel}, one that is normal to the fluid particle interfaces at the point of impact, and the tangential ones. For a given v_{rel}, the magnitude of the normal component decreases with α, rendering the collision a more 'gentle' one, which is shown to favor coalescence (Duineveld, 1994). The magnitude of the tangential component on the other hand increases with α. This increase may enhance the tangential mobility of the interfaces during the collision, which promotes the film drainage and coalescence (Ozan and Jakobsen, 2019b). However, the tangential component also limits the duration for which the two particles can stay in contact, whereas the time required for particles to coalesce could be considered to scale roughly with the inverse of the normal component. Then, a large enough α may exist, such that it would increase the coalescence time and decrease the contact time so much that coalescence becomes impossible. As evident from Fig. 4, Eq. (3) does not support such a behavior for large α and incorrectly estimates all colli-

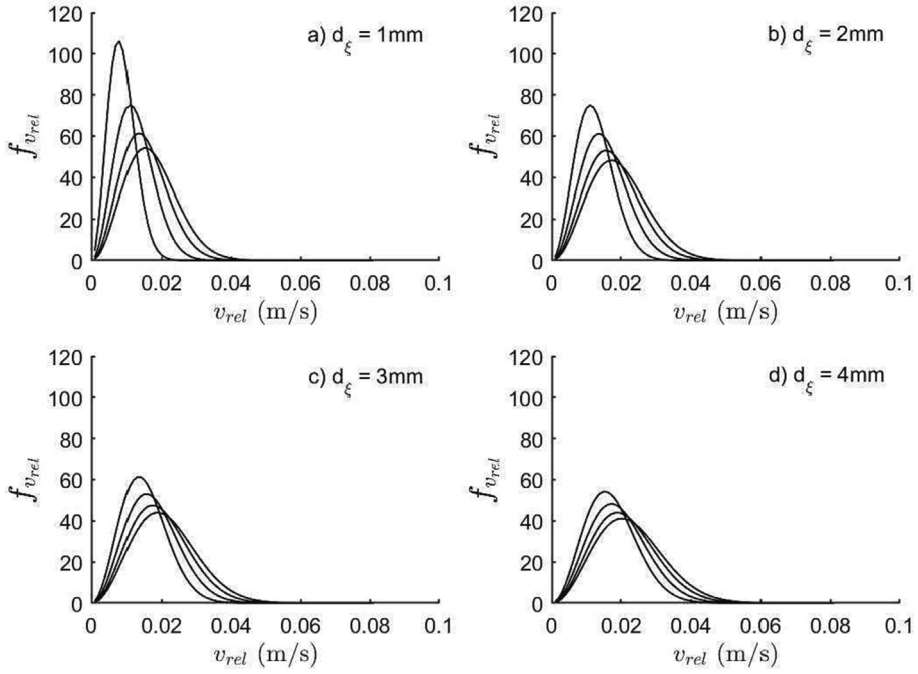

Fig. 3. Probability density function for relative velocity for $d_\eta = [1, 2, 3, 4]\,mm$ (from the leftmost to rightmost peaks) and (a) $d_\xi = 1\,mm$, (b) $d_\xi = 2\,mm$, (c) $d_\xi = 3\,mm$ and (d) $d_\xi = 4\,mm$.

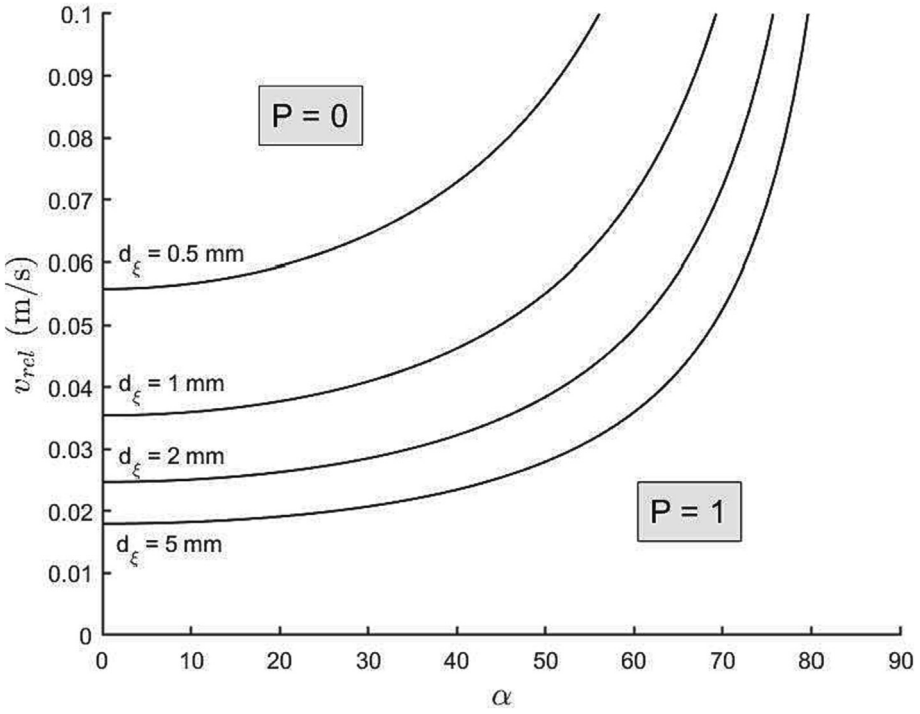

Fig. 4. Coalescence probability as a function of v_{rel} and α for $d_\eta = 1\,mm$ and $d_\xi = [0.5, 1, 2, 5]\,mm$. For each particle size couple, the corresponding curve divides the v_{rel}-α space into two: no coalescence (above the curve) and coalescence (below the curve) regions.

sions to result in coalescence regardless of v_{rel}. One way to mitigate this behavior, is to introduce an upper limit for α above which coalescence probability is set to zero. According to Rother et al. (1997) such an upper limit exists around $\alpha_u \approx 58^\circ$. The current work treats α_u as a variable model input without deviating too much from the literature value and employs Eq. (4) as the probability expression.

The joint probability density function of α and v_{rel} is presented in Fig. 5 together with its product with the coalescence probability, for $d_\eta = d_\xi = 5mm$. The largest possible collision angle for coalescence to occur is taken as $\alpha_u = 60^\circ$. As seen in Fig. 5 a), the joint probability density function is symmetrical around $\alpha = 45^\circ$ following the symmetry of $\sin(2\alpha)$, whereas no such symmetry exists with respect to v_{rel}. The product $Pf_\alpha f_{v_{rel}}$ shown in Fig. 5 b) represents the likelihood of a collision with certain α and v_{rel} to result in coalescence, after both α_u and v_c are considered. This product is only a part of the integrand for the coalescence frequency expression given in Eq. (20), and to determine $\mathbb{C}$ it should also be multiplied by the swept volume rate and be integrated over all possible v_{rel} and α values. Carrying out this integration yields a single $\mathbb{C}$ value for each particle size pair. Fig. 6 shows $\mathbb{C}$ as a function of particle sizes. For two particles of similar sizes ($d_\eta \approx d_\xi$), the results indicate that the highest coalescence frequency is obtained for $2\,mm < d_\eta < 4\,mm$ and $2\,mm < d_\xi < 4\,mm$. The non-monotonic trend along the $d_\eta \approx d_\xi$ direction can be explained through the changes in the coalescence probability and swept volume rate with particle size. When both particles are small, the coalescence probability is high due to large v_c (Eq. (1)) and relatively low attainable v_{rel} values (Fig. 3), yet low swept volume rate decreases the colli-

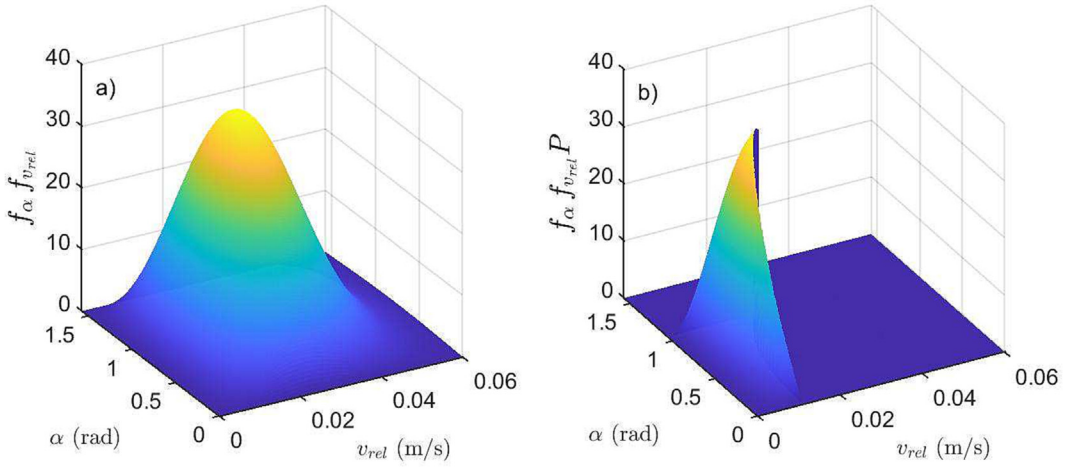

Fig. 5. Joint probability density function of α and v_{rel} in a) and its product with the coalescence probability in b) for $d_\eta = d_\xi = 5mm$. Largest collision angle allowing coalescence to happen is taken to be $\alpha_u = 60^\circ$.

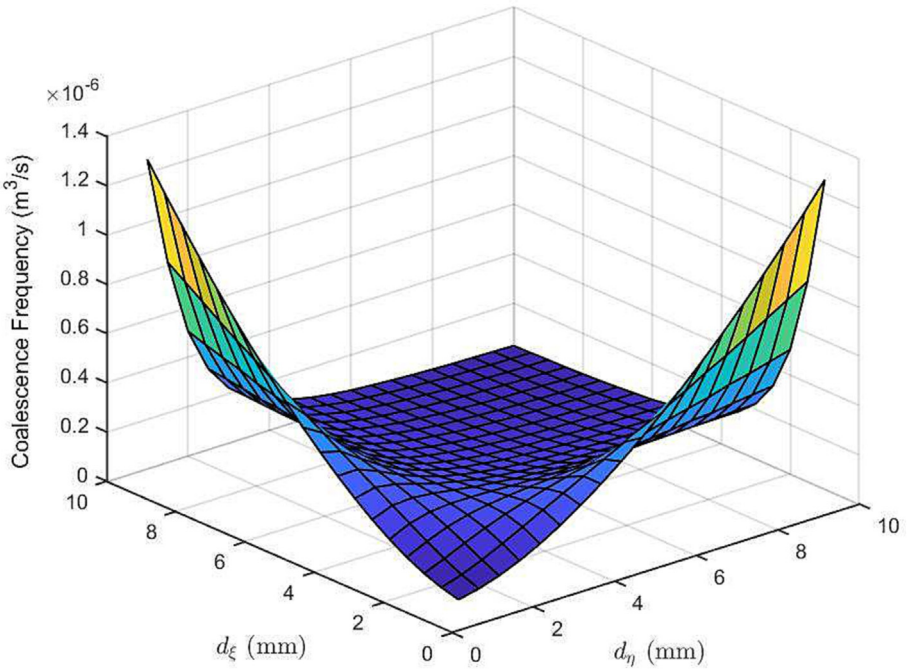

Fig. 6. Coalescence frequency $\mathbb{C}$ as a function of fluid particle size. Calculated through Eq. (20) with $\alpha_u = 60°$.

sion frequency and consequently $\mathbb{C}$. Going to the other extreme, i.e., large fluid particles, $\mathbb{C}$ diminishes once again, but this time due to the low coalescence probability (low v_c and high values of v_{rel}) despite having a larger collision frequency. Lastly, the interactions between a small fluid particle and a large one give the highest coalescence frequency. In this case, the large particle allows a high swept volume rate; whereas the small particle dominates the equivalent particle size R_p and results in large values of v_c. An increase in the difference between the particle sizes amplifies these factors and the coalescence frequency further increases.

3.2. Validation against bubbly pipe flow experiments

Next, the kernel performance is tested against three experimental cases, runs 96, 107 and 108 (Lucas et al., 2011) whose parameters are presented in Table 1. These runs have been selected purposefully, since they are coalescence dominated and show little to no breakage. The Eulerian multifluid-population balance model employed in the simulations is adapted from Solsvik and Jakobsen (2014) and the final equations are presented in Appendix B. The Eulerian equations are at steady-state and cross-sectional averaged. Furthermore, as the experimental data is coalescence dominated, the breakage terms in the model are neglected. Both the physical space (only solved in the axial direction) and the property space are discretized following a spectral scheme. The relative velocity range for the integration of Eq. (20) is taken as $[0, v_{rel,\infty}]$, where $v_{rel,\infty}$ is a large enough velocity such that $f_{v_{rel}}(v_{rel,\infty}) \to 0$. The inlet bubble size distribution in each simulation is a Gaussian distribution adjusted to fit the corresponding experimental inlet distribution. As no measurements exactly at $z = 0\,m$ are available in the experimental data sets, the distributions at $z = 0.03\,m$ are used for the fitting. The largest possible collision angle that allows coalescence, α_u, is treated as an input parameter in the vicinity of the value ($\alpha_u \approx 58°$) proposed by Rother et al. (1997).

Fig. 7 presents the comparison for run 108 for $\alpha_u = 50°$ and $\alpha_u = 60°$ at $z = 0.23\,m$ and $z = 3.03\,m$, where z is the axial coordinate along the pipe ($L_{pipe} = 3.5\,m$). The model appears to estimate the experimental behavior exceptionally, both close to the inlet and the outlet of the pipe, with only minor discrepancies between the simulation output and the experimental data. Both α_u values tested perform similarly for run 108. However, it must be noted that increasing α_u shifts the distribution slightly towards the larger bubble sizes and reduces its peak value. As can be seen from Fig. 8, the effect of α_u is much more pronounced for run 107. Although $\alpha_u = 50°$ provides an exceptional match with the experimental data, increasing α_u to 60° reveals an interesting behavior, in which the distribution begins to develop a secondary peak at a larger bubble size. This secondary peak is not in agreement with the experimental results for this particular run, but such a behavior is seen in other experiments. Specifically run 96 exhibits a very pronounced double peak distribution towards the end of the pipe, as seen in Fig. 9. The comparison for this run is not as good as the previous two sets, yet the discrepancies are still arguably small, especially for $\alpha_u = 60°$. The model manages to successfully predict the emergence of the second peak at the correct bubble size despite underpredicting f_m slightly. Furthermore, the axial position at which the second peak begins to be visible (0.83 m in the experiment) is estimated accurately by the model (between 0.9–1 m). Finally, Figs. 10 and 11 present the bubble size distribution and the Sauter mean diameter along the pipe length in all three cases for the best matching α_u values: 60° for runs 96 and 108, and 50° for run 107. The good match between the experimental and the theoretical Sauter mean diameter values in Fig. 11 imply that the current model is able to predict the experimental behavior along the pipe. All the α_u values are considerably close to each other, as well as to 58° proposed in the literature, which may suggest that α_u could have a universal value that is independent of the experimental parameters. This eventually would indicate that the proposed coalescence kernel here is devoid of any tuning parameters.

Despite the satisfactory performance of the proposed novel coalescence kernel against the experimental data, the minor discrepancies in the model prediction may be attributed to a couple factors. The critical velocity expression adapted from Ozan et al. (2021) comes from film drainage analysis, where the fluid particle

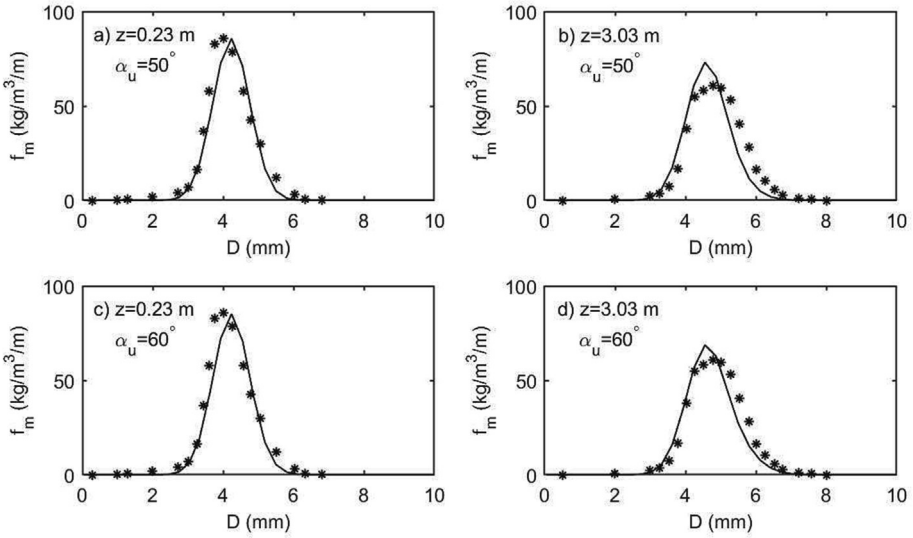

Fig. 7. Particle size distribution for run 108, close to pipe inlet (left) and close to pipe outlet (right), for different α_u. Solid lines stand for the simulation results and stars are the experimental data points.

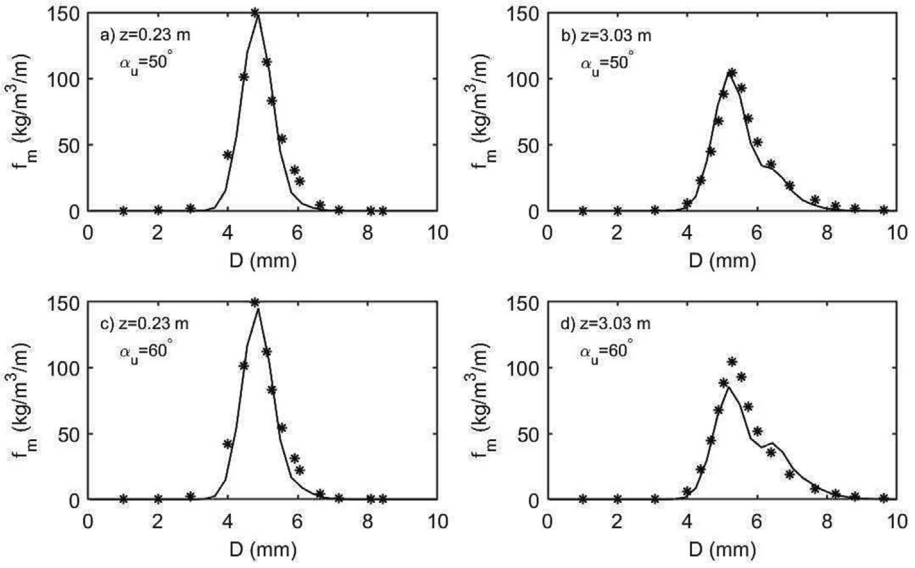

Fig. 8. Particle size distribution for run 107, close to pipe inlet (left) and close to pipe outlet (right), for different α_u. Solid lines stand for the simulation results and stars are the experimental data points.

interfaces are assumed to be immobilized. In many real systems, it is not unrealistic to expect the fluid particle interfaces to be immobile due to small amounts of impurities that are likely to be present in the system. For example, Klaseboer et al. (2000) conclude that the drainage behavior in their experiments agrees much better with a film drainage model that considers immobile interfaces than its mobile counterpart, most likely due to the presence of impurities. Yet, even though it is quite likely, there is no definitive proof showing that the bubble interfaces are completely immobilized in the experiments employed in this work for comparison. Furthermore, the film drainage model of Ozan et al. (2021) considers only axisymmetric collisions. Although the current work incorporates non-axisymmetric effects by adjusting the v_c expression for different collision angles, it is possible that such effects also play a role in the film drainage. These additional effects may result in slight changes in Eqs. (1) and (4), and ultimately impact the coalescence kernel's accuracy. While deriving the relative velocity probability function, it is assumed that the particle velocities are independent of each other, as can be seen in Appendix B. Under certain conditions, for example when wake effects are significant, this assumption may be a possible source for the discrepancy. A final remark should be made on the Eulerian multifluid-population balance used in testing. The model disregards the radial distribution of the particles inside the pipe and treats cross-sectional averaged variables, which may reduce its predictive properties. The selection of the inlet bubble size distribution's shape may also play a role in creating the discrepancy, since in the experiments the distribution may easily be different than Gaussian as assumed in the flow calculations. All these factors combined with the error in the experimental measurements may explain the discrepancies between the simulation outcome and the experimental data.

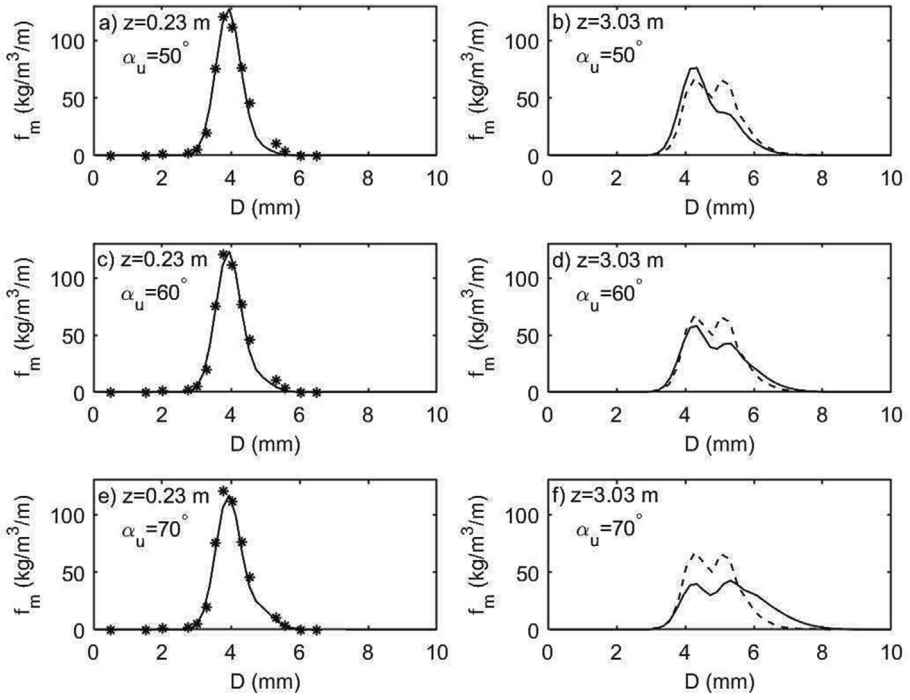

Fig. 9. Particle size distribution for run 96, close to pipe inlet (left) and close to pipe outlet (right), for different α_u. Solid lines stand for the simulation results, and stars and the dashed lines represent the experimental data.

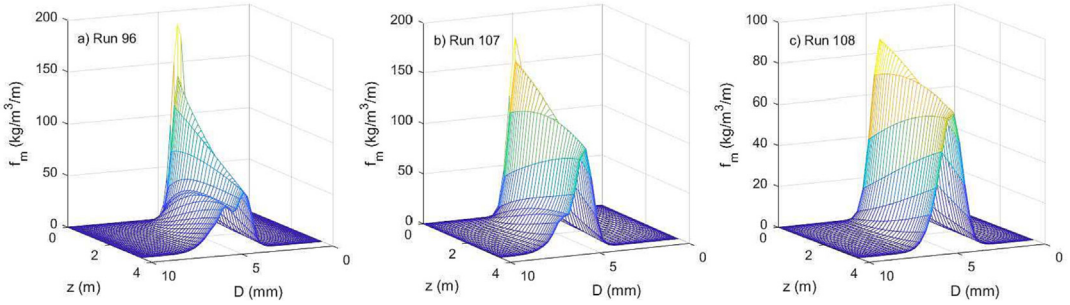

Fig. 10. Particle size distribution throughout the pipe for each run. Upper integration limit is chosen as the best fitting one, $\alpha_u = 60^\circ$ for (a) and (c), and $\alpha_u = 50^\circ$ in (b).

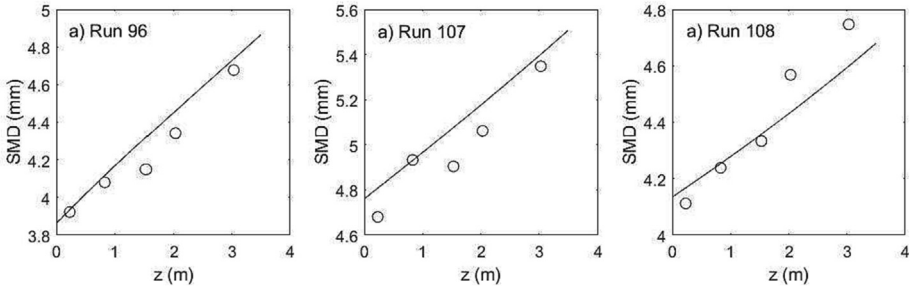

Fig. 11. Sauter mean diameter throughout the pipe for each run. Upper integration limit is chosen as the best fitting one, $\alpha_u = 60^\circ$ for a) and c), and $\alpha_u = 50^\circ$ in b).

4. Conclusions

This work constructs a novel coalescence kernel to be employed within the population balance framework. The kernel includes a coalescence probability expression that stems from the critical velocity estimations of Ozan et al. (2021)'s film drainage simulations. While sharing the merits of the existing literature models (film drainage based, energy, and critical velocity models), the proposed kernel avoids inheriting their drawbacks. Furthermore, it is free of any artificially introduced tuning parameters. In adaptation to the Eulerian frame, the collision relative velocity and the collision angle are treated as distributed parameters through probability density functions. The model's development is finalized with the addition of a factor signifying the largest possible collision angle that allows coalescence. The performance of the resulting kernel is tested against bubbly pipe flow experiments, and show

exceptional agreement with multiple runs. The model is able to reproduce the experimental bubble size distribution successfully, including more complex behaviors such as distributions with double-peak.

Declaration of Competing Interest

The authors declare that they have no known competing financial interests or personal relationships that could have appeared to influence the work reported in this paper.

Acknowledgements

We thank Dr. Roland Rzehak from Helmholtz-Zentrum Dresden-Rossendorf for valuable and fruitful discussions.

Appendix A. Appendix A

This appendix is dedicated to derivation of the probability density function of the relative velocity between the fluid particles (Eq. (5)). The derivation starts with Eq. (2.16) of Wilczek et al. (2011), where the probability density function of the velocity vector $\mathbf{v}$ and its magnitude v are related through:

$$\tilde{f}(v) = 4\pi v^2 f(\mathbf{v}) \tag{21}$$

Through their analysis, Wilczek et al. (2011) show that these two functions are normal distributed and end up with the following expressions for the probability density functions in their Eqs. (2.50) and (2.51):

$$\tilde{f}(v) = \sqrt{\frac{2}{\pi}}\frac{v^2}{\sigma^3}\exp\left(-\frac{1}{2}\frac{v^2}{\sigma^2}\right) \tag{22}$$

$$f(\mathbf{v}) = \frac{1}{(2\pi\sigma^2)^{3/2}}\exp\left(-\frac{1}{2}\frac{\mathbf{v}\cdot\mathbf{v}}{\sigma^2}\right) \tag{23}$$

The validity of Eqs. (22) and (23) is shown and discussed in their Figs. 3 and 4. However, it must be noted that these equations are valid for a single fluid particle and further manipulations are needed for the relative velocity density function of two particles. Such manipulations have been previously discussed in the literature, e.g by Das (2015) and Gong et al. (2018), yet for the sake of completeness they are revisited and discussed here. By denoting the particle velocities with $\mathbf{v}_\xi$ and $\mathbf{v}_\eta$, and by assuming their distributions are independent of each other, a joint probability density can be written as

$$\begin{aligned} f(\mathbf{v}_\xi,\mathbf{v}_\eta) = f(\mathbf{v}_\xi)f(\mathbf{v}_\eta) &= \frac{1}{(2\pi\sigma_\xi^2)^{\frac{3}{2}}}\exp\left(-\tfrac{1}{2}\frac{\mathbf{v}_\xi\cdot\mathbf{v}_\xi}{\sigma_\xi^2}\right)\frac{1}{(2\pi\sigma_\eta^2)^{\frac{3}{2}}}\exp\left(-\tfrac{1}{2}\frac{\mathbf{v}_\eta\cdot\mathbf{v}_\eta}{\sigma_\eta^2}\right) \\ &= \frac{1}{(2\pi)^3\sigma_\xi^3\sigma_\eta^3}\exp\left(-\tfrac{1}{2}\frac{\mathbf{v}_\xi\cdot\mathbf{v}_\xi}{\sigma_\xi^2}-\tfrac{1}{2}\frac{\mathbf{v}_\eta\cdot\mathbf{v}_\eta}{\sigma_\eta^2}\right) \end{aligned} \tag{24}$$

Each particle velocity is then decomposed into the relative velocity $\mathbf{v}_{rel}$ and the remainder $\mathbf{w}$ as

$$\mathbf{v}_\xi = \frac{\sigma_\xi^2}{\sigma_\xi^2+\sigma_\eta^2}\mathbf{v}_{rel} + \frac{\sigma_\xi\sigma_\eta}{\sigma_\xi^2+\sigma_\eta^2}\mathbf{w} \tag{25}$$

$$\mathbf{v}_\eta = -\frac{\sigma_\eta^2}{\sigma_\xi^2+\sigma_\eta^2}\mathbf{v}_{rel} + \frac{\sigma_\xi\sigma_\eta}{\sigma_\xi^2+\sigma_\eta^2}\mathbf{w} \tag{26}$$

where $\mathbf{v}_{rel} = \mathbf{v}_\xi - \mathbf{v}_\eta$. Then the expression can be rewritten as

$$f(v_{rel},w) = \frac{1}{(2\pi)^3\sigma_\xi^3\sigma_\eta^3}\exp\left(-\frac{1}{2}\frac{v_{rel}^2+w^2}{\sigma_\xi^2+\sigma_\eta^2}\right) \tag{27}$$

where $v_{rel} = \sqrt{\mathbf{v}_{rel}\cdot\mathbf{v}_{rel}}$ and $w = \sqrt{\mathbf{w}\cdot\mathbf{w}}$. Next, the expression is integrated in the velocity space for $dv_{\xi,x}dv_{\xi,y}dv_{\xi,z}dv_{\eta,x}dv_{\eta,y}dv_{\eta,z}$ to cover all the directions. Here $x_i = x,y,z$ are the Cartesian coordinates. A transformation between the particle velocity components and the relative velocity components yield

$$dv_{\xi,i}dv_{\eta,i} = \frac{\sigma_\xi\sigma_\eta}{\sigma_\xi^2+\sigma_\eta^2}dw_i dv_{rel,i} \tag{28}$$

where the factor on the right-hand-side is the Jacobian of the transformation. Then, in the differential form, the function becomes

$$\begin{aligned} f(v_{rel},w) &= \frac{1}{(2\pi)^3\sigma_\xi^3\sigma_\eta^3}\exp\left(-\tfrac{1}{2}\frac{v_{rel}^2+w^2}{\sigma_\xi^2+\sigma_\eta^2}\right)dv_{\xi,x}dv_{\xi,y}dv_{\xi,z}dv_{\eta,x}dv_{\eta,y}dv_{\eta,z} \\ &= \frac{1}{(2\pi)^3\sigma_\xi^3\sigma_\eta^3}\exp\left(-\tfrac{1}{2}\frac{v_{rel}^2+w^2}{\sigma_\xi^2+\sigma_\eta^2}\right)\left(\frac{\sigma_\xi\sigma_\eta}{\sigma_\xi^2+\sigma_\eta^2}\right)^3 dw_x dv_{rel,x}dw_y dv_{rel,y}dw_z dv_{rel,z} \\ &= \frac{1}{(2\pi)^3\left(\sigma_\xi^2+\sigma_\eta^2\right)^3}\exp\left(-\tfrac{1}{2}\frac{v_{rel}^2+w^2}{\sigma_\xi^2+\sigma_\eta^2}\right)dw_x dv_{rel,x}dw_y dv_{rel,y}dw_z dv_{rel,z} \end{aligned} \tag{29}$$

Writing Eq. (29) in terms components in spherical coordinates r,θ,ϕ gives

$$f(v_{rel},w) = \frac{v_{rel}^2\sin\phi_{v_{rel}}w^2\sin\phi_w}{(2\pi)^3\left(\sigma_\xi^2+\sigma_\eta^2\right)^3}\exp\left(-\frac{1}{2}\frac{v_{rel}^2+w^2}{\sigma_\xi^2+\sigma_\eta^2}\right)d\phi_{v_{rel}}d\theta_{v_{rel}}dv_{rel}d\phi_w d\theta_w dw$$

as $dv_{rel,x}dv_{rel,y}dv_{rel,z} = v_{rel}^2\sin\phi_{v_{rel}}d\phi_{v_{rel}}d\theta_{v_{rel}}dv_{rel}$ and $dw_x dw_y dw_z = w^2\sin\phi_w d\phi_w d\theta_w dw$. Then, by integrating for all the possible states (from 0 to 2π in $\theta_{v_{rel}}$ and θ_w, 0 to π in $\phi_{v_{rel}}$ and ϕ_w, and 0 to ∞ in w), the relative velocity probability density function is obtained as

$$f_{v_{rel}} = \frac{4\pi v_{rel}^2}{\left[2\pi\left(\sigma_\xi^2+\sigma_\eta^2\right)\right]^{3/2}}\exp\left(-\frac{1}{2}\frac{v_{rel}^2}{\sigma_\xi^2+\sigma_\eta^2}\right) \tag{31}$$

Appendix B. Appendix B

Solsvik and Jakobsen (2014) present a combined Eulerian multifluid-population balance model for bubbly flow consisting of the momentum balance for each phase, the continuous phase continuity equation and the population balance equation. The cross-sectional averaged population balance equation at steady-state reads

$$\begin{aligned} &\tfrac{\partial}{\partial z}\left[v_{d,z}(D,z)f_m(D,z)\right] - \tfrac{f_m(D,z)v_{d,z}(D,z)}{\rho_d(z)}\tfrac{\partial\rho_d(z)}{\partial z} \\ &+\tfrac{\partial}{\partial D}\left[v_{d,D}(D,z)f_m(D,z)\right] - \tfrac{3}{D}v_{d,D}(D,z)f_m(D,z) \\ &= D_B(D,z) + B_B(D,z) + D_C(D,z) + B_C(D,z) \end{aligned} \tag{32}$$

where D is the particle size, z is the axial direction in the pipe and f_m is the mass density of fluid particles within the continuous phase. The axial dispersed phase velocities in the physical and in the property spaces are respectively denoted by $v_{d,z}$ and $v_{d,D}$. The right-hand size terms stand for the death and birth terms due to coalescence and breakage, and are expressed as

$$D_B(D,z) = -b(D)f_m(D,z) \tag{33}$$

$$B_B(D,z) = V(D)\int_D^{D_{\max}} h(D,D\prime)b(D\prime)\frac{f_m(D\prime,z)}{V(D\prime)}\,\mathrm{d}D\prime \tag{34}$$

$$D_C(D,z) = -f_m(D,z)\int_{D_{\min}}^{\left(D_{\max}^3-D^3\right)^{1/3}}\mathbb{C}(D,D\prime)\frac{f_m(D\prime,z)}{\rho_d(z)V(D\prime)}\,\mathrm{d}D\prime \tag{35}$$

$$B_C(D,z) = \frac{D^2 V(D)}{2} \int_{D_{\min}}^{\left(D^3 - D_{\min}^3\right)^{1/3}} \frac{\mathbb{C}\left(\left[D^3 - D\prime^3\right]^{1/3}, D\prime\right)}{\left[D^3 - D\prime^3\right]^{2/3}} \times \frac{f_m(D\prime,z)}{\rho_d(z) V(D\prime)} \frac{f_m\left(\left[D^3 - D\prime^3\right]^{1/3}, z\right)}{V(D) - V(D\prime)} \mathrm{d}D\prime \tag{36}$$

where $D\prime$ is the size of the secondary particle, V is the particle volume, b denotes the breakage frequency function and h is the daughter size distribution function. The dispersed and the continuous phase momentum equations are given

$$\frac{\partial}{\partial z}\left[f_m(D,z)\, v_{d,z}(D,z)\, v_{d,z}(D,z)\right] = -\frac{\partial}{\partial D}\left[f_{d,m}(D,z)\, v_{d,z}(D,z)\, v_{d,D}(D,z)\right] - \frac{f_m(D,z)}{\rho_d(z)} \frac{\mathrm{d}p(z)}{\mathrm{d}z} + f_m(D,z) g + f_{drag} \tag{37}$$

$$\alpha_c(z)\rho_c v_c(z) \frac{\mathrm{d}}{\mathrm{d}z} v_c(z) = -\alpha_c(z) \frac{\mathrm{d}p(z)}{\mathrm{d}z} - \frac{\alpha_c(z)\rho_c f_w(z)}{2D_{pipe}} v_c(z)^2 + \alpha_c(z)\rho_c g - \int_{D_{\min}}^{D_{\max}} f_{\mathrm{drag}}(D,z)\, \mathrm{d}D \tag{38}$$

where f_{drag} is the drag force, α_c is the volume fraction of the continuous phase, g is the gravitational acceleration and f_w is the wall friction factor. The closures for the drag and the friction terms can be found in Table 1 of Solsvik and Jakobsen (2014). Finally, the continuity equation gives

$$\frac{\mathrm{d}}{\mathrm{d}z}\left(\alpha_c(z)\rho_c(z) v_c(z)\right) = 0 \tag{39}$$

for the continuous phase.

References

Bazhlekov, I.B., Chesters, A.K., Van de Vosse, F.N., 2000. The effect of the dispersed to continuous-phase viscosity ratio on film drainage between interacting drops. Int. J. Multiph. Flow 26 (3), 445–466.

Coulaloglou, C.A., 1975. Dispersed Phase Interactions in an Agitated Flow Vessel. Illinois Institute of Technology.

Das, S.K., 2015. Development of a coalescence model due to turbulence for the population balance equation. Chem. Eng. Sci. 137, 22–30.

Duineveld, P.C., 1994. Bouncing and coalescence phenomena of two bubbles in water. In: Bubble Dynamics and Interface Phenomena. Springer, Dordrecht, pp. 447–456.

Duineveld, P.C., 1998. Bouncing and coalescence of bubble pairs rising at high Reynolds number in pure water or aqueous surfactant solutions. In: Fascination of Fluid Dynamics. Springer, Dordrecht, pp. 409-439.

Gong, S., Han, L., Luo, H.A., 2018. A novel multiscale theoretical model for droplet coalescence induced by turbulence in the framework of entire energy spectrum. Chem. Eng. Sci. 176, 377–399.

Kamp, A.M., Chesters, A.K., Colin, C., Fabre, J., 2001. Bubble coalescence in turbulent flows: A mechanistic model for turbulence-induced coalescence applied to microgravity bubbly pipe flow. Int. J. Multiph. Flow 27 (8), 1363–1396.

Klaseboer, E., Chevaillier, J.P., Gourdon, C., Masbernat, O., 2000. Film drainage between colliding drops at constant approach velocity: experiments and modeling. J. Colloid Interface Sci. 229 (1), 274–285.

Lehr, F., Millies, M., Mewes, D., 2002. Bubble-size distributions and flow fields in bubble columns. AIChE J. 48 (11), 2426–2443.

Liao, Y., Lucas, D., 2010. A literature review on mechanisms and models for the coalescence process of fluid particles. Chem. Eng. Sci. 65 (10), 2851–2864.

Lucas, D., Krepper, E., Prasser, H.M., 2005. Development of co-current air–water flow in a vertical pipe. Int. J. Multiph. Flow 31 (12), 1304–1328.

Lucas, D., Liao, Y., Markelov, I., 2011. Air-water experiments in a vertical DN50 pipe. Helmholtz-Zentrum Dresden-Rossendorf (internal report).

Ozan, S.C., Jakobsen, H.A., 2019a. On the effect of the approach velocity on the coalescence of fluid particles. Int. J. Multiph. Flow 119, 223–236.

Ozan, S.C., Jakobsen, H.A., 2019b. On the role of the surface rheology in film drainage between fluid particles. Int. J. Multiph. Flow 120, 103103.

Ozan, S.C., Hosen, H.F., Jakobsen, H.A., 2021. On the prediction of coalescence and rebound of fluid particles: A film drainage study. Int. J. Multiph. Flow 135, 103521.

Rother, M.A., Zinchenko, A.Z., Davis, R.H., 1997. Buoyancy-driven coalescence of slightly deformable drops. J. Fluid Mech. 346, 117–148.

Solsvik, J., 2017. Turbulence modeling in the wide energy spectrum: explicit formulas for Reynolds number dependent energy spectrum parameters. Eur. J. Mech.-B/Fluids 61, 170–176.

Solsvik, J., Jakobsen, H.A., 2014. Bubble coalescence modeling in the population balance framework. J. Dispers. Sci. Technol. 35 (11), 1626–1642.

Solsvik, J., Jakobsen, H.A., 2016. A review of the statistical turbulence theory required extending the population balance closure models to the entire spectrum of turbulence. AIChE J. 62 (5), 1795–1820.

Sovova, H., 1981. Breakage and coalescence of drops in a batch stirred vessel–II comparison of model and experiments. Chem. Eng. Sci. 36 (9), 1567–1573.

Wilczek, M., Daitche, A., Friedrich, R., 2011. On the velocity distribution in homogeneous isotropic turbulence: correlations and deviations from Gaussianity. J. Fluid Mech. 676, 191–217.

Zhao, W., Wang, H., Bai, R., Wei, W., Wang, H., 2021. Bubble characteristics and turbulent dissipation rate in horizontal bubbly pipe flow. AIP Adv. 11 (2), 025125.